Electronic Supplementary Material (ESI) for Energy & Environmental Science.

Supporting Information (SI)

Green Transformation of CO_2 to Ethanol using Water and Sunlight by Cooperative Endeavour of Naturally Abundant Red Phosphorus and Bi_2MoO_6

Risov Das,[a,b] Kousik Das,[a,b] Bitan Ray,[a,b] Chathakudath P. Vinod,[c] Sebastian C. Peter*[a,b]

[a]*New Chemistry Unit, Jawaharlal Nehru Centre for Advanced Scientific Research, Jakkur, Bangalore-560064*

[b]*School of Advanced Materials, Jawaharlal Nehru Centre for Advanced Scientific Research, Jakkur, Bangalore-560064*

[c]*Catalysis and Inorganic Chemistry Division, CSIR-National Chemical Laboratory, Dr. Homi Bhabha Road, Pune, 410008*

Supplementary Note

Experimental Section

1. Synthesis

1.1 Chemical: The following chemicals were used: Red Phosphorus (P, Sigma Aldrich), ethylene glycol [$(CH_2OH)_2$, Sigma Aldrich], bismuth nitrate pentahydrate [$Bi(NO_3)_3\cdot5H_2O$, Alfa Aesar], sodium molybdate dihydrate [$Na_2MoO_4\cdot2H_2O$, Alfa Aesar]. All the chemicals are commercially available certified reagents and used without further purification.

1.2 Synthesis of Bi_2MoO_6 by solvothermal method: Stochiometric amount of $Bi(NO_3)_3\cdot5H_2O$, $Na_2MoO_4\cdot2H_2O$ were immersed in 15 mL of ethylene glycol and 15 ml of hot water respectively, and then were mixed together. The resulting suspension was maintained at 160 °C for 24 h in a 45 mL Teflon-lined autoclave. Finally, the products were washed thoroughly with deionized water and dried in vacuum oven at 60° C for 10 hours.

1.3 Synthesis of exfoliated red phosphorus (RP): Commercially available RP was sonicated for 20h in water to get exfoliated RP.

1.4 Synthesis of RP/Bi_2MoO_6 heterostructures by solvothermal method: Exfoliated RP and previously synthesised Bi_2MoO_6 was sonicated together for 12 hours. Finally, the composites were dried at 60 °C for 6 h to get RP/Bi_2MoO_6 powders. The weight ratio of RP and Bi_2MoO_6 was varied from 1:1 to 3:1 to get different composites. The composite with 1:1, 2:1 and 3:1 weight ratio was named as **RP-BMO(11), RP-BMO(21)** and **RP-BMO(31)**. We have used the same nomenclature throughout the manuscript.

2. Characterization

2.1 X-Ray Diffraction: The structural phase of pristine Bi_2MoO_6, RP and composites were confirmed by X–ray diffraction (XRD, Rigaku Advance X-ray diffractometer equipped with Cu kα lamp source for irradiation 1.5 Å). As depicted in **Fig. S1b** for RP, low angle peak at 2θ = 16° is matching with reported literature.[1] In the case of Bi_2MoO_6, the diffraction peaks observed at 28.25°, 32.59°, 33.07°, 46.72°, 47.07°, 55.46°, 55.53° and 56.16° can be perfectly indexed to the (131), (002), (060), (202), (260), (331), (133), and (191) planes of orthorhombic Bi_2MoO_6 ($Pca2_1$). For RP/Bi_2MoO_6 compositess all the peaks can be assigned to Bi_2MoO_6, along with a hump at around 16° corresponding to RP (**Fig. S1b)**. The hump intensity has been decreased with an increasing amount of Bi_2MoO_6. Absence of any other extra peak proves the purity of the phase.

2.2 Microscopy: To understand morphology of material high-resolution transmission electron microscopy (HRTEM) was taken. Sample preparation was done by drop casting small amount of sonicated powder in ethanol on a carbon coated copper grid. SEM images were taken by FEI NOVA NANOSEM 600 scanning electron microscope equipped with an energy-dispersive X-ray spectroscopy (EDAX) instrument (Bruker 129 eV EDAX instrument). Data was acquired by using an accelerating voltage of 20 kV and typical time taken for data accumulation is 100 s. The elemental analyses were performed using the P/B-ZAF standardless method (where, P/B = peak to background model, Z = atomic no. correction factor, A = absorption correction factor and F = fluorescence factor) for C, N, O, Co at multiple areas on the sample coated Si wafer.

2.3 Photoluminescence (PL): PL spectra of all the solid samples were recorded at room temperature on a steady state Luminescence spectrometer Perkin-Elmer (LS 55) at different excitation wavelength.

2.4 The ultraviolet-visible diffuse reflectance spectrum (UV-vis DRS): UV-vis spectra were obtained in the range of 250 to 800 nm by using a Perkin-Elmer Lambda 900 UV/Vis/Near- IR spectrophotometer in reflectance mode for Bi_2MoO_6, RP and other composites with an integrating sphere attachment. $BaSO_4$ was used as a 100% reflectance standard. The absorption was calculated data using the Kubelka−Munk equation,[2] $\alpha/S = (1 - R)^2/2R$, where R is the reflectance and α and S are the absorption and scattering coefficients, respectively. Band gap was derived using Tauc plot.

2.5 X-ray photoelectron spectroscopy (XPS):

XPS data were obtained using Omicron Nanotechnology spectrometer using an Al-Kα. All the binding energies were referenced to the C 1*s* peak at 284.8 eV.

2.6 Surface area measurement:

Specific surface area measurements were performed on BELSORP-MR6 by adsorption of nitrogen gas at – 77 K, applying the Brunauer-Emmett-Teller (BET) calculation.[3] Prior to adsorption analysis, the samples were degassed at 85 °C for 12h. Pore size distributions were derived from desorption isotherms using Barrett-Joyner-Halenda (BJH) method.

3. Photocatalytic Measurements

A quartz photoreactor was used for CO_2 hydrogenation experiment under the illumination of 450 W xenon lamp (with UV cut-off filter (KG-2 filter and CGA-400) filter) solar simulator. About 5 mg of the sample was well dispersed in 20 mL of water by ultrasonication. Before

illumination, the reaction setup was purged with N_2 to remove the air and then purged with high purity CO_2 for 45 minutes.
During irradiation, 3 mL of the gaseous product from the setup was sampled, and gas analysis study was done by GC (gas chromatography) (Agilent GC-7890 B) with TCD and FID detector and He carrier gas. Blank tests were conducted in the absence of CO_2 and light to confirm that these two factors are key for photocatalytic CO_2 reduction reaction. Rate of the evolved gases were calculated after at 10-hour reaction.
Liquid product analysis: The liquid products were analysed by and HPLC (Agilent 1220 Infinity II LC system) and GC-MS (Agilent). After each cycle, catalytic system was purged with N_2 for 40 minutes followed by fresh batch of CO_2 purging.

Control studies was done with UV grade ultra-pure methanol and CD_3OD using same photocatalytic setup for 10h. Control study with methane was done by maintaining similar procedure as CO_2 reduction. However, the purging was done by CH_4 instead of CO_2.

Calculation of relative quantum yield (QY) rate ratio for ethanol production

AQY of RP-BMO(21) for photocatalytic CO_2 reduction reaction were calculated for simulated light source and sunlight. KG-2 filter CGA-400 filter were used to cut off UV and IR part of the simulated light (450 W xenon lamp from Newport). The light intensity was measured using a power meter (Newport-843-R) the intensity of outputting light was measured. The intensity of Xe lamp ($P_{Xe\ lamp}$) is 116 mW/cm^2 and sunlight ($P_{direct\ sunlight}$) is 84 mW/cm^2.

$$QY(\%) = \frac{Number\ of\ reacted\ electrons\ for\ ethanol\ formation}{Number\ of\ incident\ photons} X\ 100\%$$

Number of reacted electrons were calculated from the yield of CO_2 reduced products. Because different number of electrons are required for the formation of different products, the total number of reacted electrons are

$$Number\ of\ reacted\ electrons\ for\ ethanol\ formation = \left[12n(CH_3CH_2OH)\right] X\ N_A$$

$n(CH_3CH_2OH)$ is the rate of ethanol formation in moles/g/h, respectively. N_A is Avogadro's number.

Number of incident photons are calculated from the following equation:

$$Number\ of\ incident\ photons = \frac{PSt}{hc}$$

where, P is the power density of the incident light (W/m^2), S (m^2) is the irradiation area, t (s) is the duration of the incident light exposure.

Combining these two equations the ratio of QY(%) were calculated for ethanol formation rate under direct sunlight and simulated light (Xe lamp).

$$QY(\%)\ rate\ ratio = \frac{Rate\ of\ Ethanol\ formation\ under\ direct\ sunlight\ X\ P_{Xe\ lamp}}{Rate\ of\ Ethanol\ formation\ under\ Xe\ lamp\ X\ P_{direct\ sunlight}} \times 100\%$$

$$= \frac{34.1}{51.8} \times \frac{116}{84} \times 100\%$$

$$= 90.91\%$$

4. In-situ Photocatalytic Fourier Transform Infrared Spectroscopy (FT-IR):

In-situ photochemical FT-IR spectroscopic studies were performed using a purged VERTEX FT-IR spectrometer equipped with the A530/P accessory and a mid-band Mercury Cadmium Telluride (MCT) detector. Spectra were recorded after 100 scans with a resolution of 4 cm^{-1}. A DRIFTS cell with a quartz window was used to perform catalytic experiment. Prior to catalytic testing, 5 mg of the sample was placed in the DRIFTS cell and treated in flowing N_2 for 30 min to remove impure gas mixtures. Then, CO_2 and water vapor were injected through rubber septa and light was illuminated through the quartz window for 100 minutes. Just before the light exposure on the DRIFTS cell the zero-minute data was collected and followed by data under light was collected every 10 minutes for 100 minutes.

5. Time resolved photoluminescence:

Photoluminescence decay profiles were recorded using a Horiba Delta Flex time correlated single-photon-counting (TCSPC) instrument. A 520 nm laser diode with a pulse repetition rate of 1 MHz was used as the light source. The instrument response function (IRF) was collected using a scatterer (Ludox AS40 colloidal silica, Sigma-Aldrich)

6. Photoelectrochemical Measurements:

The transient photocurrent measurements under dark and light were done in a three-electrode system using a CHI 760 potentiostat under the illumination of a solar simulator (Newport) with an ultraviolet (UV) ($\lambda > 380$ nm) cut-off filter. Ag/AgCl was reference electrode, and platinum as the counter electrode was used. All samples were spin coated on fluorine-doped tin oxide (FTO) which were used as working electrode. 0.5 M Na_2SO_4 was taken as electrolyte. The slurry was prepared by adding 10 mg of the sample, 200 μL of Nafion (5%), and 1 mL of isopropyl alcohol to fabricated photoelectrodes. The obtained paste was spin-coated on FTO with 1 cm^2 area and annealed at 100 °C for 1 h to get a homogenous film. Mott-Schottky (MS) plots were recorded at a scan rate of 10 mV/s in Na_2SO_4 neutral solution in the light at a frequency of 50 kHz. The obtained values (w.r.t Ag/AgCl) was converted w.r.t NHE by adding 0.20 V.

Supplementary tables

Table S1. Overall CO_2 reduction performance by different RP/Bi_2MoO_6 composite photocatalysts. Rate of product formation was given in μmol g^{-1} h^{-1} unit. ND: No product was detected (beyond detection limit)**.** BMO(AS) means BMO after sonication.

Sample	**Methane**	**Formic acid**	**Methanol**	**Ethanol**
RP-BMO(31)	10.2	17.7	7.1	8.4
RP-BMO(21)	11.3	19.6	30.2	51.8
RP-BMO(11)	8.1	10.2	24.6	28.4
RP-BMO(12)	3.3	7.3	11.2	6.4
RP	7.2	9.6	6.2	ND
Bi_2MoO_6	0.71	0.89	1.03	0.42
Bi_2MoO_6(AS)	**1.37**	**1.23**	**1.98**	**1.31**

Table S2. CO_2 to ethanol formation by photocatalytic route. Comparison of ethanol formation rate by RP-BMO(21) with reported literature.

Entry	**Catalyst**	**Product**	**Yield (μmol$g^{-1}h^{-1}$)**	**Light source, Reaction mode**	**References**
1	RP-BMO(21)	CH_3CH_2OH	51.8 (Xe lamp) 34.1 (Sunlight)	Xe lamp (450W), Solid-liquid	This work
2	AgBr–NG–g-C_3N_4	CH_3CH_2OH	51	Xe lamp (450W), Solid-liquid	[4]
3	Cu^{2+} doped TiO_2	CH_3CH_2OH	47	365 nm LED lamp, Solid-vapour	[5]
4	$BiVO_4$	CH_3CH_2OH	22	Xe lamp (300 W) Solid-liquid (continuous gas flow).	[6]
5	Pt and N co-doped hollow hierarchical BiOCl	CH_3CH_2OH CH_3OH	14.2	Xe lamp (300 W) Solid-liquid (0.1M NaOH solution, continuous gas flow)	[7]
6	Conducting polymers modified Bi_2WO_6 microspheres	CH_3CH_2OH	5.13	Xe lamp (300 W) Solid -liquid	[8]
7	MoS_2/Bi_2WO_6 nanocomposites	CH_3CH_2OH	9.15	Xe lamp (300 W) Solid -liquid	[9]
8	Bi_2MoO_6 quantum dots in situ grown on reduced graphene	CH_3CH_2OH	14.37	0.47 W/cm^2, Solid-liquid (continuous gas flow)	[10]

	oxide layers				
9	Red Ag/AgCl	CH_3CH_2OH	44.6	Xe lamp (500 W) Solid-liquid (0.1M $NaHCO_3$ solution, continuous gas flow)	11
10	ZnO/g-C_3N_4	CH_3CH_2OH	1.5	Xe lamp (500 W) Solid-liquid (continuous gas flow)	12
11	WS_2 /Bi_2S_3	CH_3CH_2OH CH_3OH	6.95 9.55	Xe lamp (300 W) Solid -liquid	13
12	$LaVO_4$	CH_3CH_2OH CH_3OH	12.7 1.20	Xe lamp (300 W) Solid -liquid CO_2-saturated $NaHCO_3$ solution containing 0.2 M Na_2SO_3	14
13	STO/Cu@Ni/TiN	CH_3CH_2OH	21.3	Xe lamp (300 W) Solid -liquid	15
14	Bi_4TaO_8Cl/Bi	CH_3CH_2OH CH_3OH	5.11 2.34	Xe lamp (300 W) Solid -liquid Photothermal	16
15	Bi_2MoO_6/PVP	CH_3CH_2OH CH_3OH	4.7 6.2	Xe lamp (300 W) Solid -liquid	17

Table S3. Parameters of the TRPL decay. The data was fitted using the following equation.

$A+B1\exp(-t/\tau_1)+B2\exp(-t/\tau_2)+B3\exp(-t/\tau_3)$), where, B1, B2, and B3 are the pre-exponential factor (amplitude) corresponding to decay lifetimes τ_1, τ_2, and τ_3 respectively. Here $\tau_{avg.}$ is the average life time and χ is goodness of fit.[18]

Sample	τ_1 (ns)	B1	τ_2 (ns)	B2	τ_3 (ns)	B3	$\tau_{avg.}$ (ns)	χ^2
comp21	0.85	0.58	2.73	0.26	16.65	0.16	3.87	1.17
Bi_2MoO_6	0.32	0.38	2.7	0.47	10	0.15	2.8	1.10

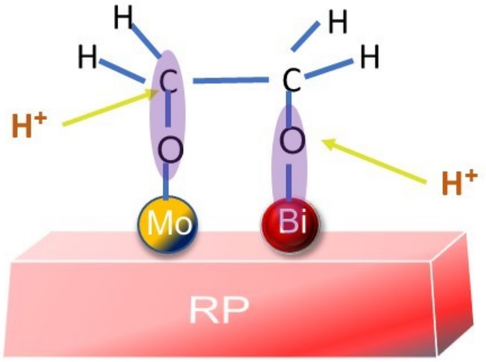

Scheme S1. Schematic representation of protonation on C centre (Mo-OC*) and O centre (Bi-O*).

Figures

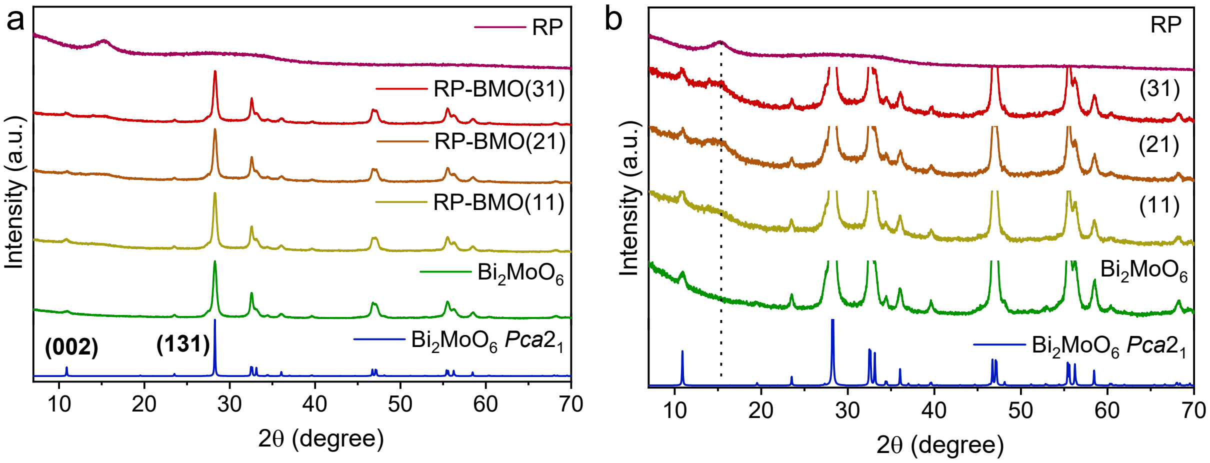

Fig. S1 | Powder X-ray diffraction (PXRD) patterns. a, Phase purity characterization by PXRD of **RP**, **RP-BMO(31)**, **RP-BMO(21)**, **RP-BMO(11)** and Bi_2MoO_6. The line showed along (131) plane indicates, there is no shift of peak position upon composite formation. **b**, zoomed version of Fig. S1a for showing the presence of amorphous red phosphorus (RP).

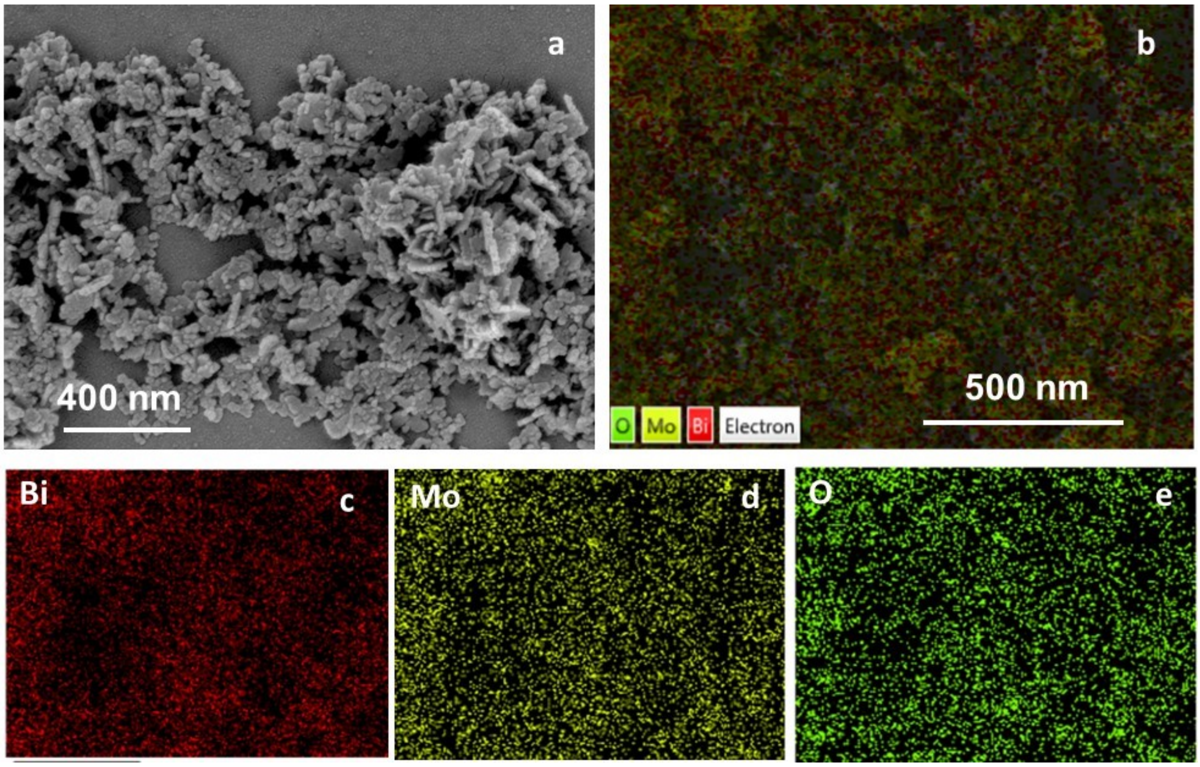

Fig. S2 | SEM images and color mapping of Bi_2MoO_6. a. SEM images of pristine Bi_2MoO_6 nano particles. **b-e**, SEM elemental mapping projecting a superimposition **(b)** of the distribution of bismuth **(c)**, molybdenum **(d)**, oxygen **(e)**.

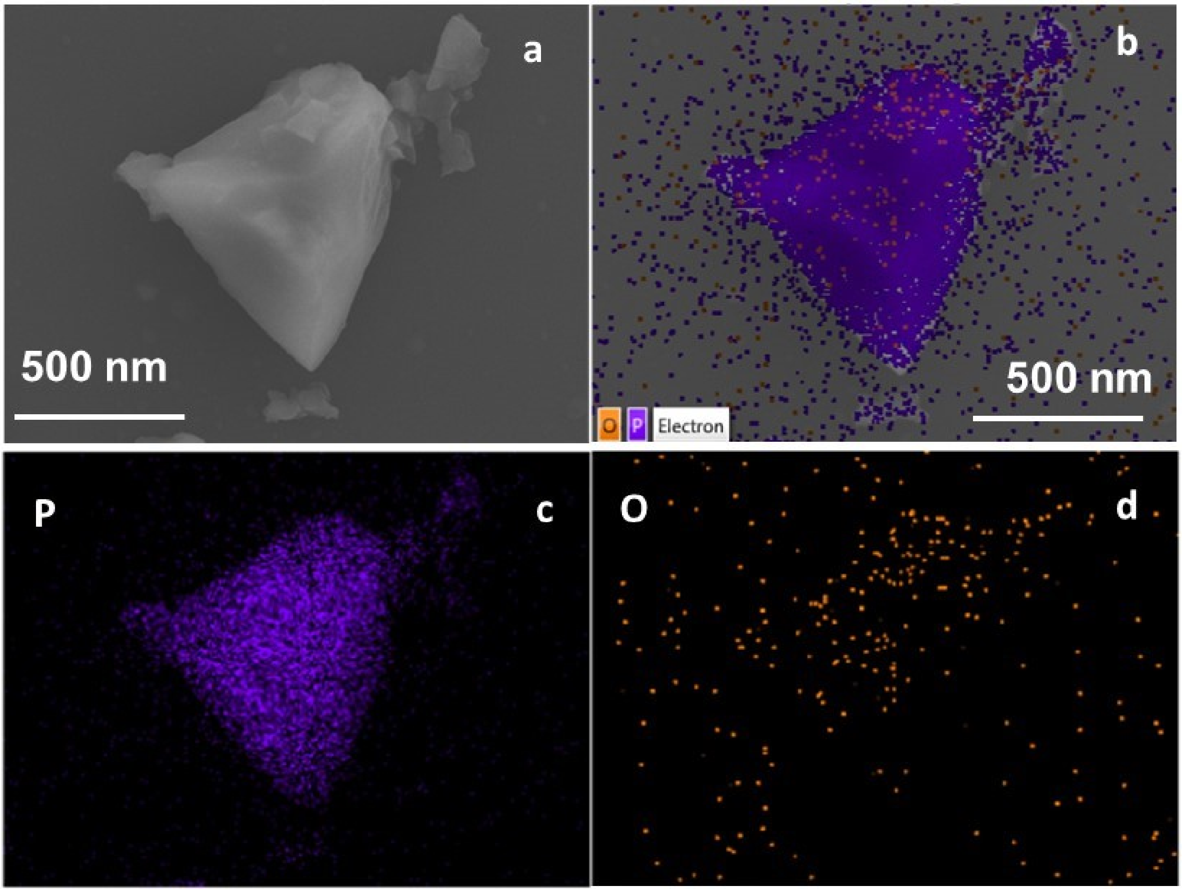

Fig. S3 | SEM images and color mapping of red phosphorus. a. SEM images of pristine red phosphorus (RP). **b-d**, SEM elemental mapping displaying a superimposition **(b)** of the distribution of phosphorus **(c)**, oxygen **(d).** Absence of oxygen eliminates the surface oxidation of phosphorus and the formation phosphorus oxide compounds.

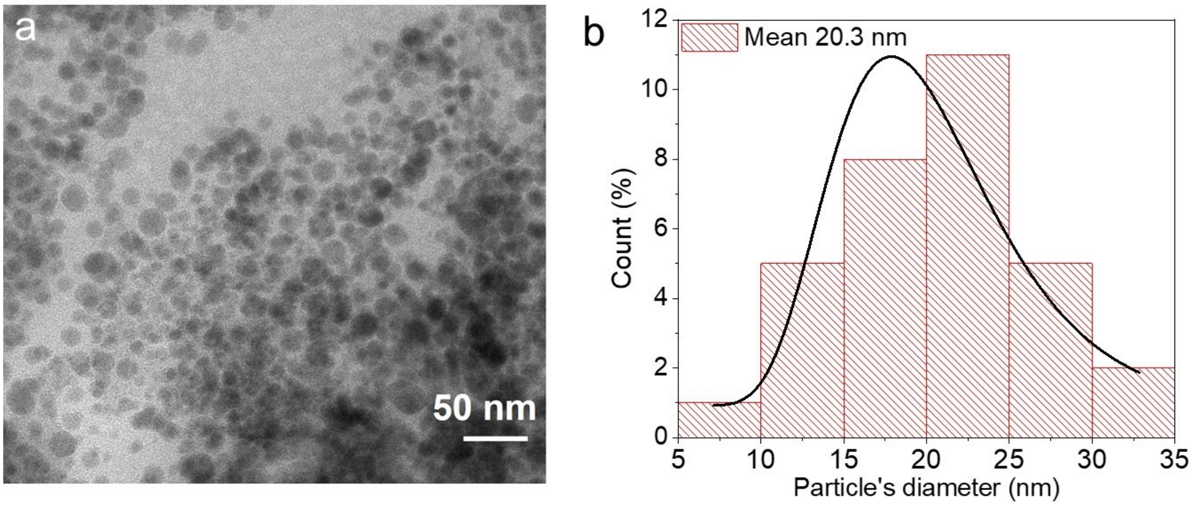

Fig. S4 | TEM images of pristine BMO. a, TEM images showed uniform spherical BMO nanoparticle. **b**, Particle size of BMO nanoparticle were calculated from **fig. S4 a**.

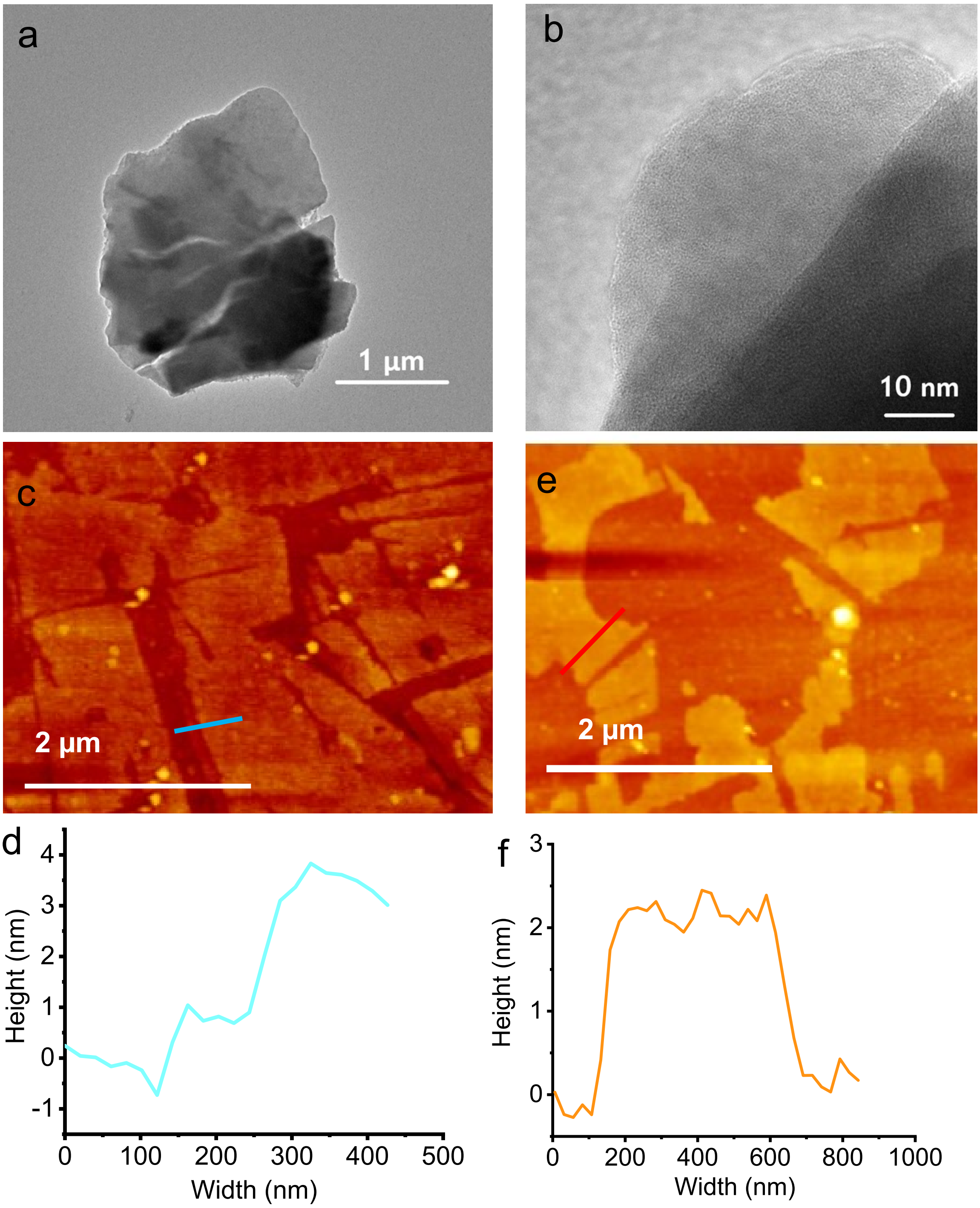

Fig. S5 | Microscopic images of exfoliated RP. a, TEM and, **b**, HRTEM image of exfoliated RP. **c**, AFM image and, **d**, height profile of 10h sonicated RP. 2 layers of RP can be seen from image and height profile both. **e**, AFM image and, **f**, height profile of 20h sonicated single layer RP. The layers of RP are around 2 nm.

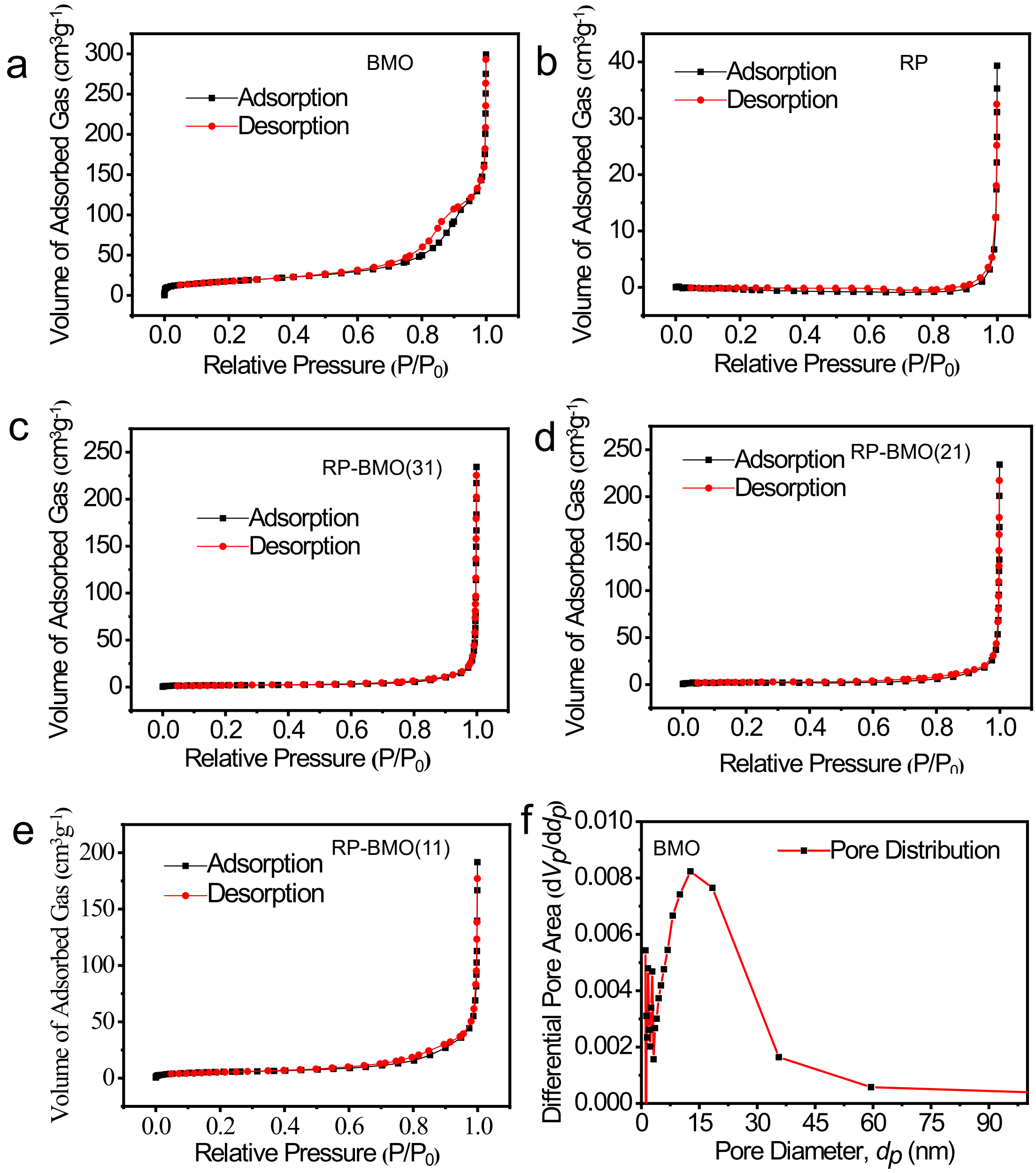

Fig. S6 | BET measurements of Bi_2MoO_6/RP composite and individual components. a-e, N_2 adsorption-desorption isotherms of RP **(a)**, **RP-BMO(31) (b)**, **RP-BMO(21) (c)**, **RP-BMO(11) (d)**, Bi_2MoO_6 **(e)**. **f**, Mesopore size distribution of Bi_2MoO_6.

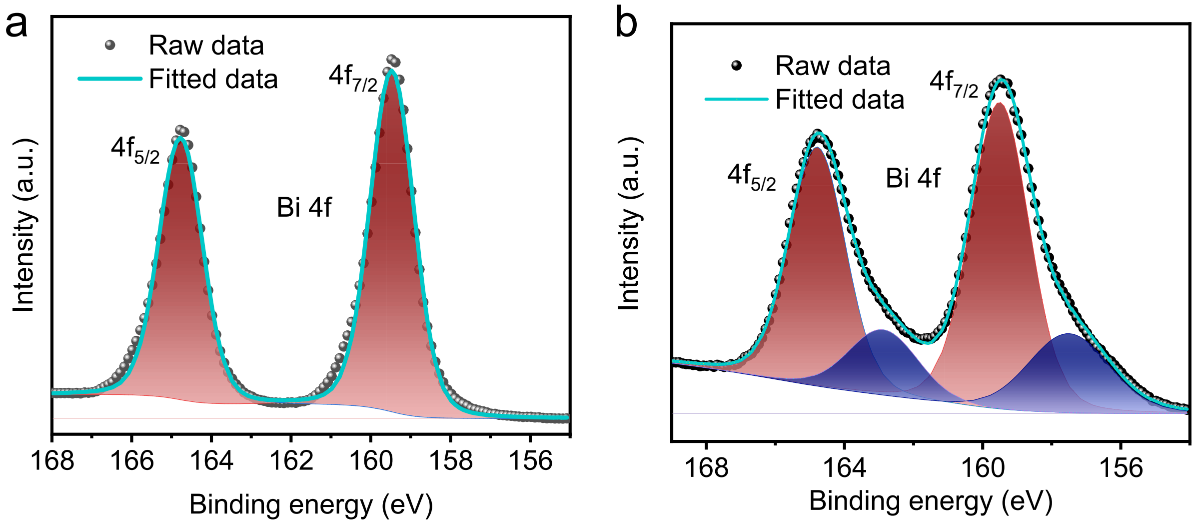

Fig. S7 | XPS measurements. a, Bi 4f spectra corresponds to Bi^{3+} in pristine BMO. **b**, Bi 4f spectra corresponds to Bi^{3+} (red) and Bi^{0} (blue) in RP-BMO (21).

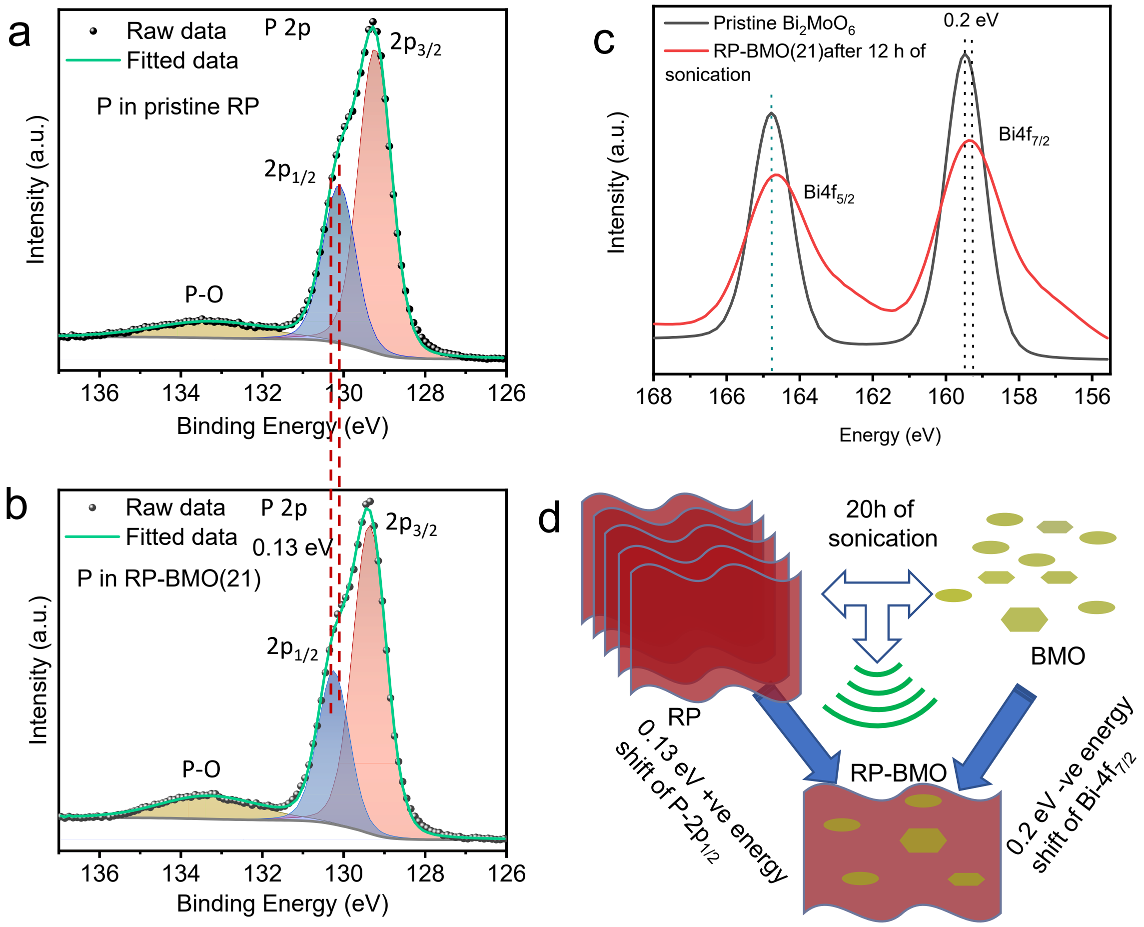

Fig. S8 | XPS analysis for understanding electronic interaction between BMO and RP. (**a-b**), Higher energy shift in P-2p XPS in RP-BMO(21) compared to pristine RP. **c**, Lower energy shift of Bi-4f XPS in RP-BMO(21) compared to pristine BMO. **d**, Schematic representation of RP-BMO composite formation due to sonication and its impact on XPS binding energy shift.

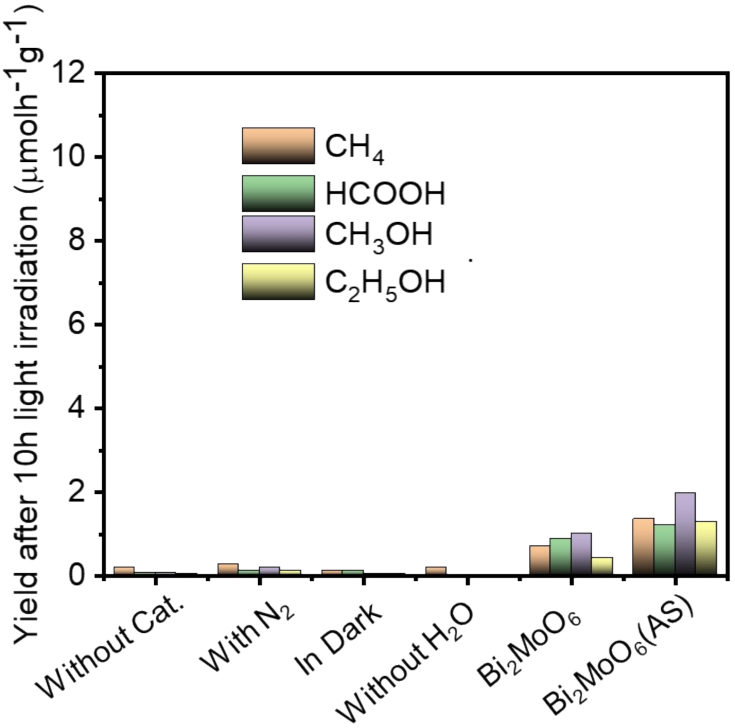

Fig. S9 | Photocatalytic control experiments. Experiments were done in absence of catalyst, CO_2, light and water. Pristine Bi_2MoO_6 showed very feeble photocatalytic performance.

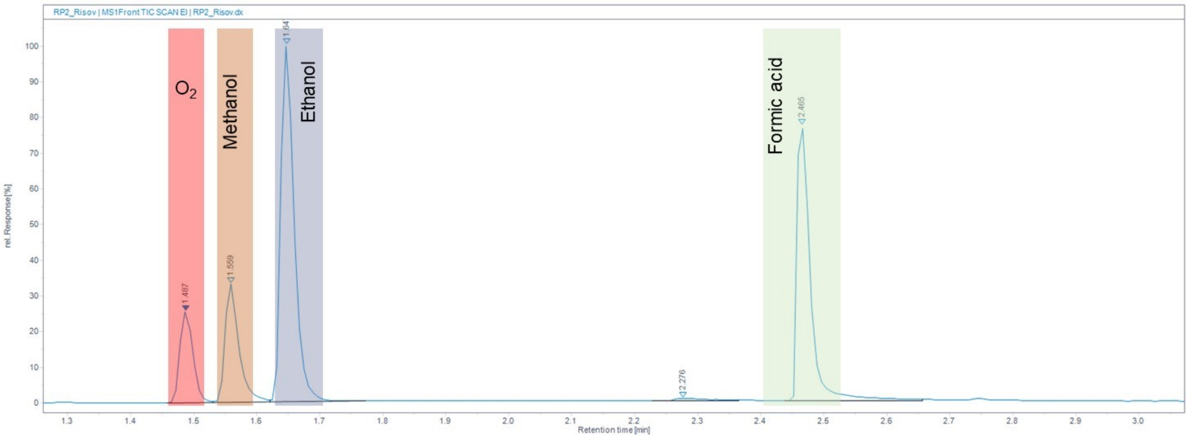

Fig. S10 | Screenshot taken from GC. Liquid products were analyze by GC after the catalysis with RP-BMO(21).

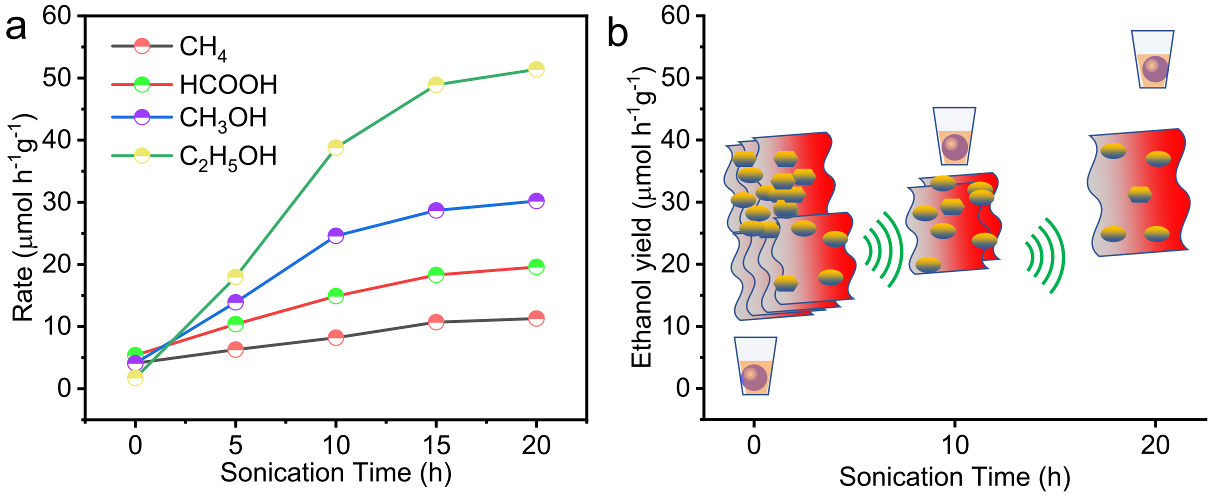

Fig. S11 | Effect of sonication on catalysis. (a) Photocatalytic CO_2 reduction activity of RP-BMO(21) upon different interval of sonication. (b) Schematic representation of effect of sonication in separating RP sheets and its corelation with ethanol formation efficiency.

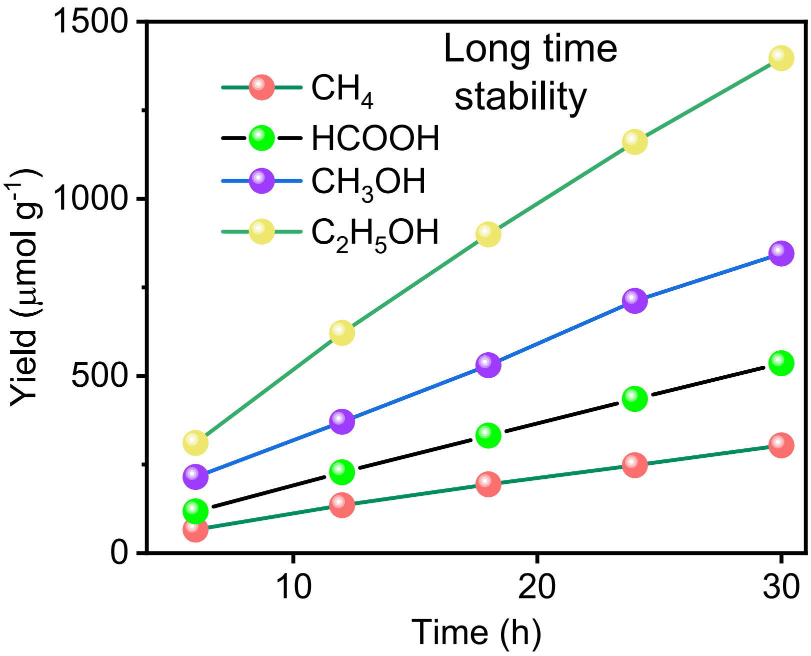

Fig. S12 | 30 h stability tests with RP-BMO(21) catalyst where data collections were done after each 6h.

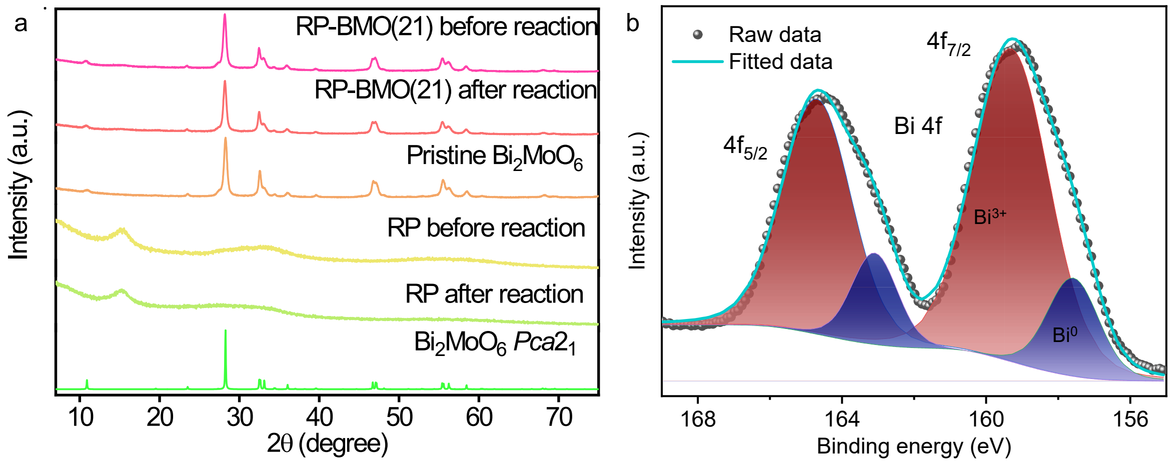

Fig. S13 | Stability test of the catalysts after reaction. a, XRD was taken before and after the photocatalytic tests (5 cycles). Phase purity and stability of pristine RP was also checked by recording XRD patterns before and after the photocatalytic reactions. **b**, XPS of RP-BMO(21) sample taken after photocatalytic CO_2 RR studies.

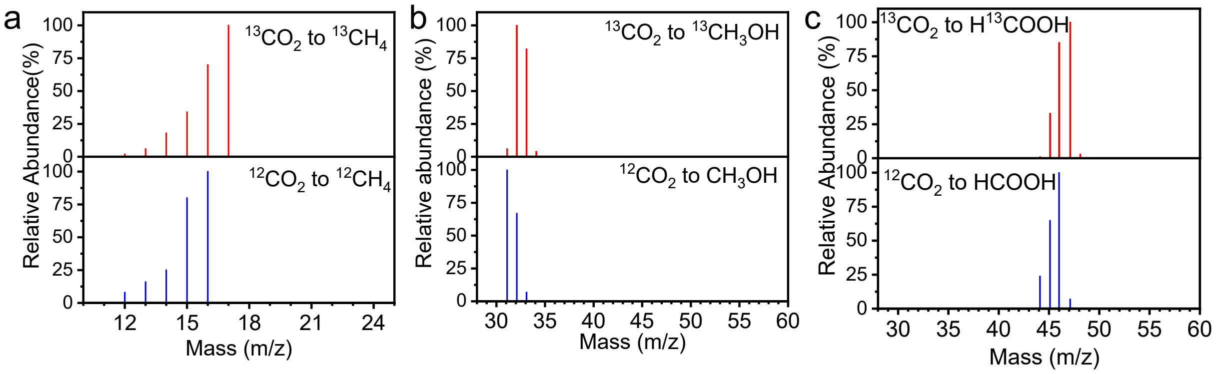

Fig. S14 | Product analysis by GC-MS after the reaction with RP-BMO(21) catalyst. MS of (a) $^{13}CH_4$, (b) $^{13}CH_3OH$, (c) $H^{13}COOH$ obtained upon the reactions with $^{13}CO_2$.

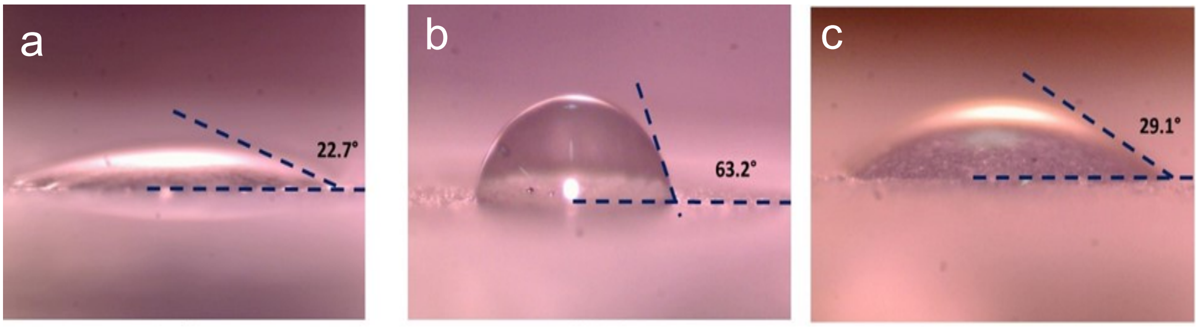

Fig. S15 | Surface wettability measurements. **a-c**, Static contact angles of water droplets on the surface of RP **(a)**, Bi_2MoO_6 **(b)**, RP-BMO(21) **(c).** These contact angles indicate RP has best hydrophilic surface.

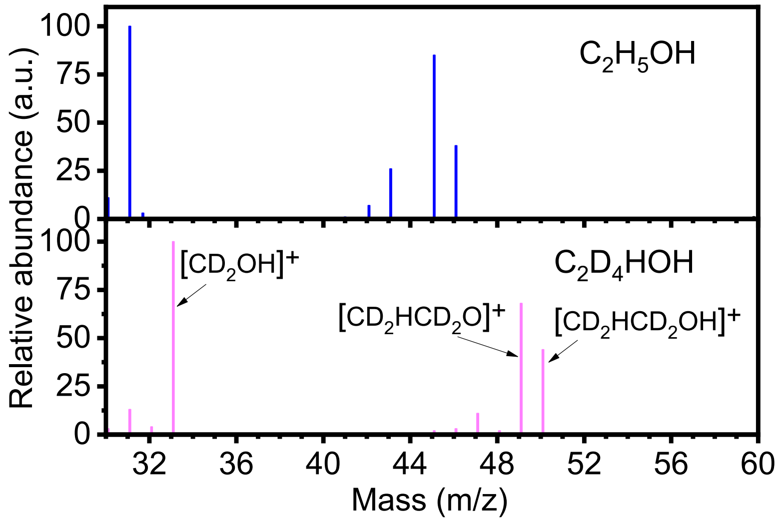

Fig. S16 | MS of ethanol obtained from CD_3OD after reaction with RP-BMO(21). Deuterated methanol converted to ethanol on RP-BMO(21) catalyst upon light illumination.

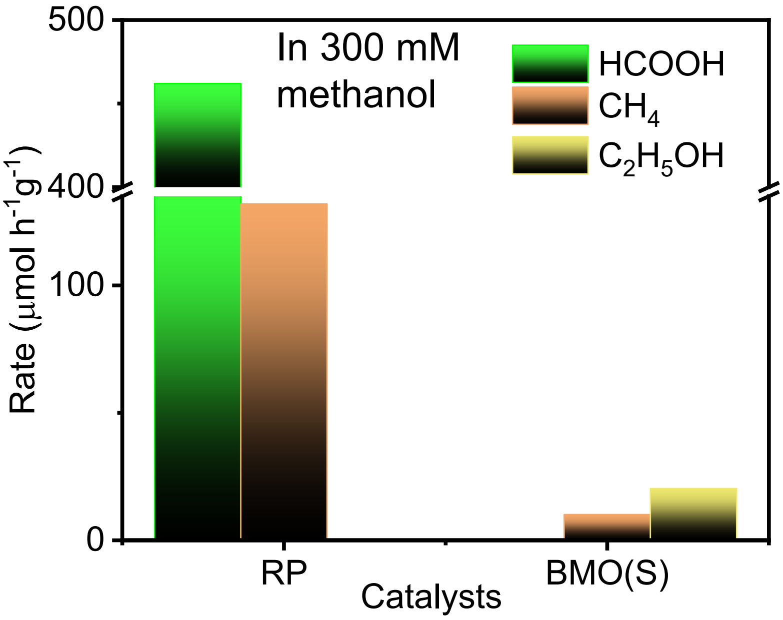

Fig. S17 | Photocatalytic activity of exfoliated red phosphorus (RP) and 20h sonicated Bi_2MoO_6 (BMO(AS), AS means after sonication) when 300 mM methanol was used as reactant. The reaction was carried out for 10h.

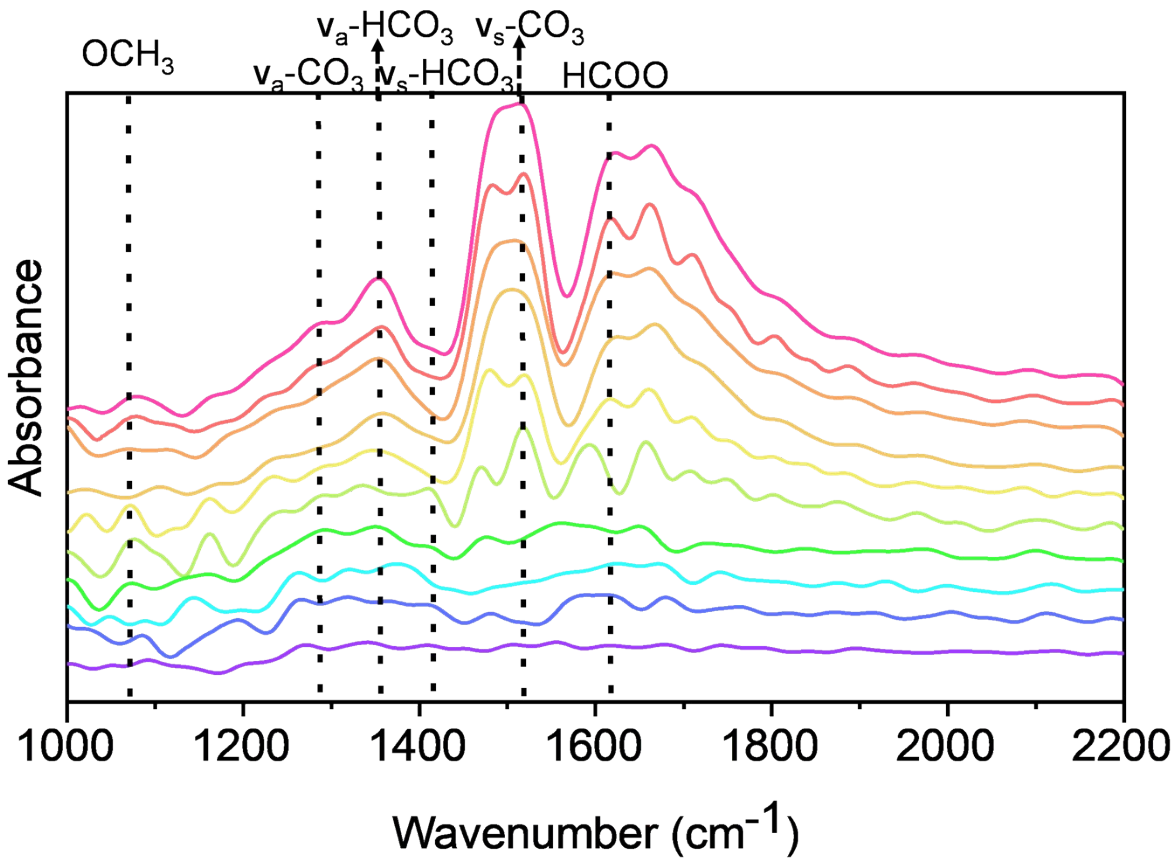

Fig. S18 | In-situ Diffuse Reflectance Infrared Fourier Transform Spectroscopy (DRIFTS) measurements of Bi_2MoO_6. In situ FTIR spectra recorded for Bi_2MoO_6 under light illumination after purging the in situ cell with adequate amount of CO_2 and water vapour.

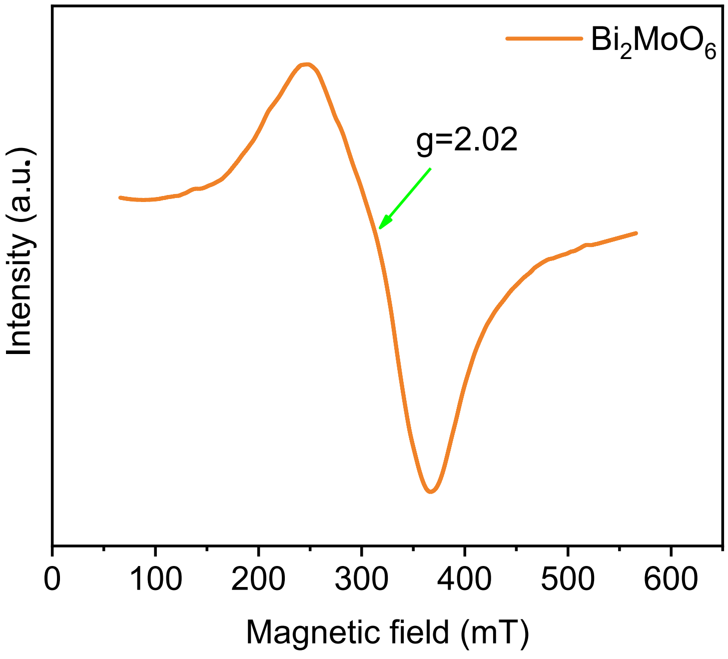

Fig. S19 | Characterization of oxygen vacancy in Bi_2MoO_6. Presence of weak ESR signal (at g=2.02) indicates the presence of some oxygen vacancy in Bi_2MoO_6.

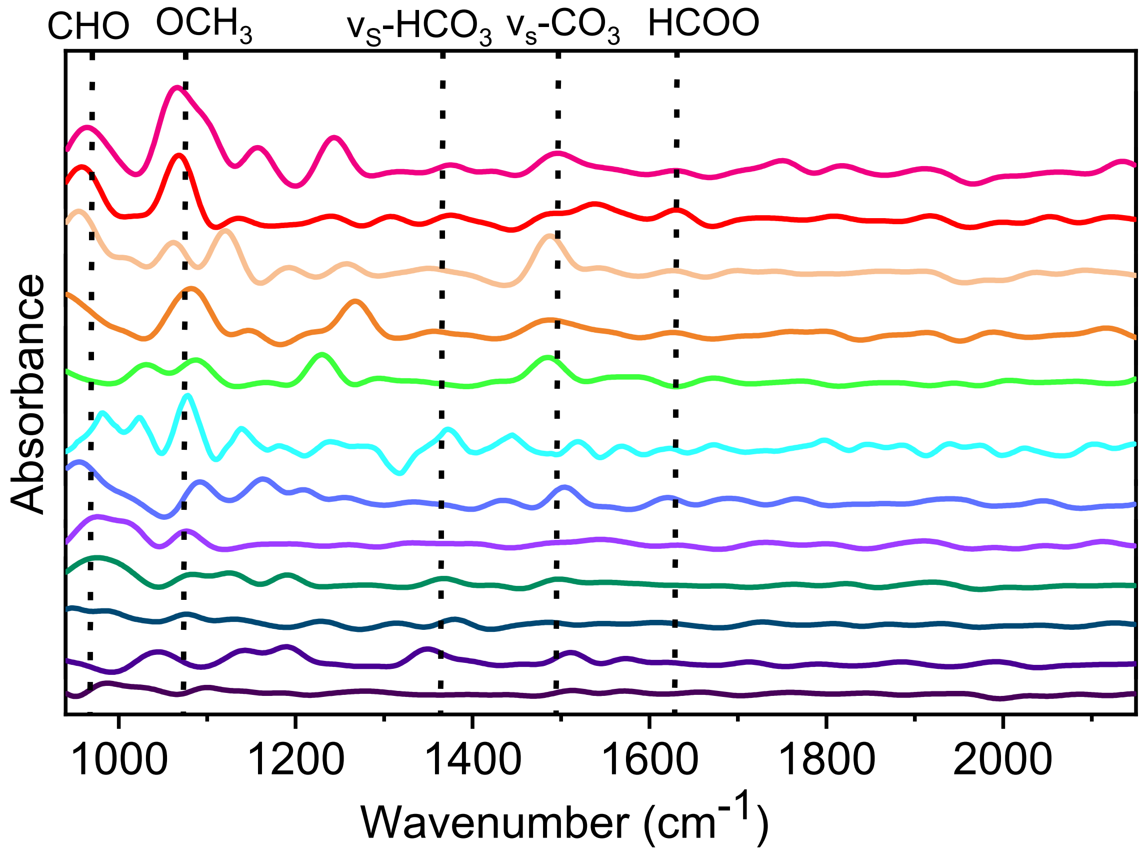

Fig. S20 | In-situ (DRIFTS) measurements of RP. In situ FTIR spectra recorded under light illumination after purging the in situ cell with adequate amount of CO_2 and water vapour.

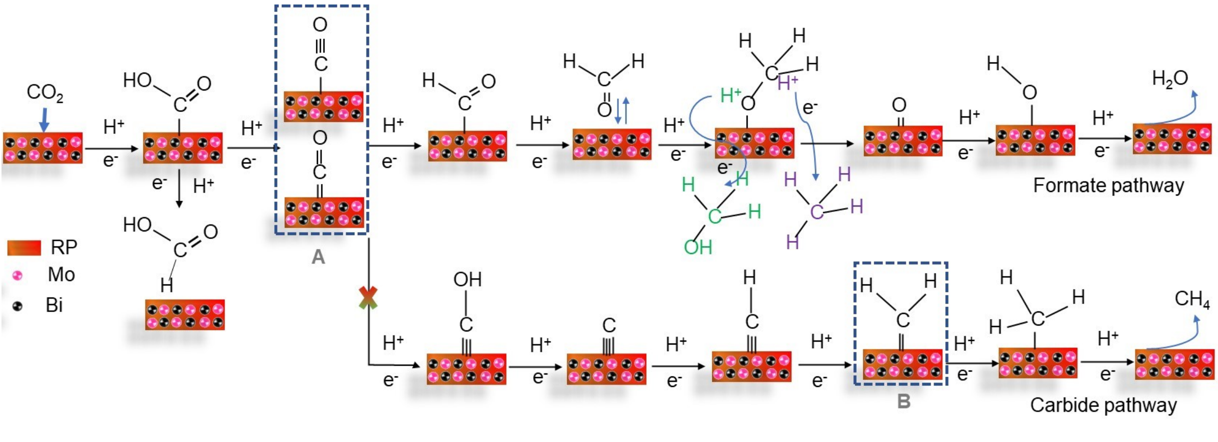

Fig. S21 | Plausible reaction pathways for CO_2 to C1 product formation. CO_2 to formic acid, methanol and methane formation mechanism by formate pathway (top) upon light irradiation. Selective methane formation by carbide mechanism (bottom) from CO_2 photoreduction.

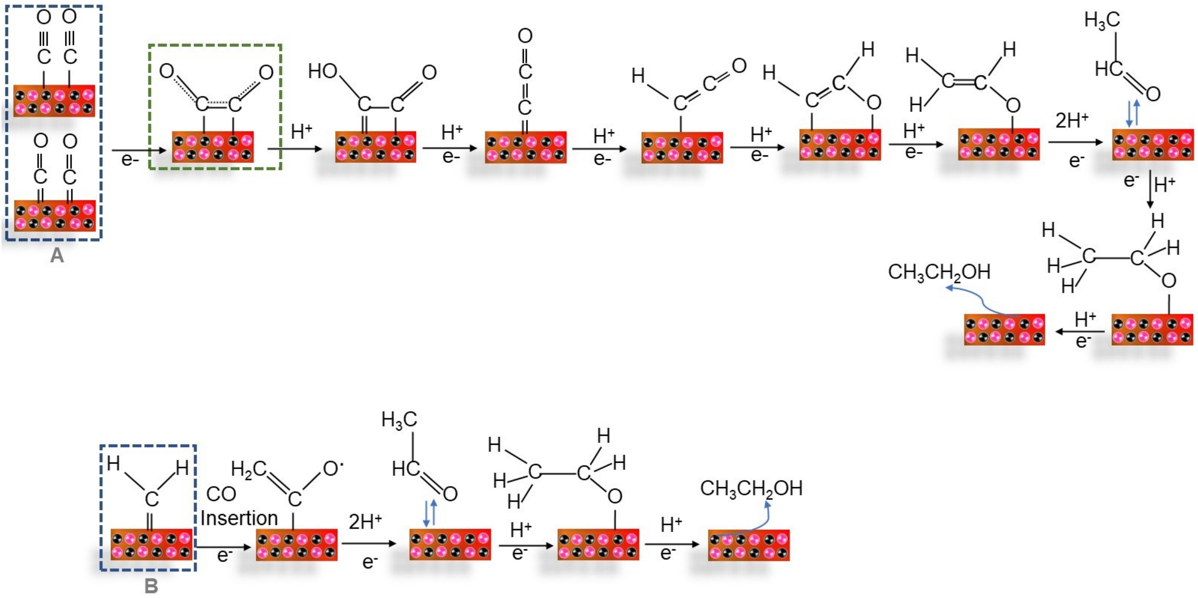

Fig. S22 | Plausible photocatalytic reaction pathways for CO_2 to ethanol formation. Coupling of 2 CO* (as shown by the dotted box (A) in Fig. S13) leads to the formation of acetaldehyde followed by the conversion to ethanol by proton coupled electron transfer pathway (top). Ethanol formation by CO insertion into M-CH_2* (depicted by the dotted box(B) in Fig. S13) which was obtained from carbide mechanism (bottom).

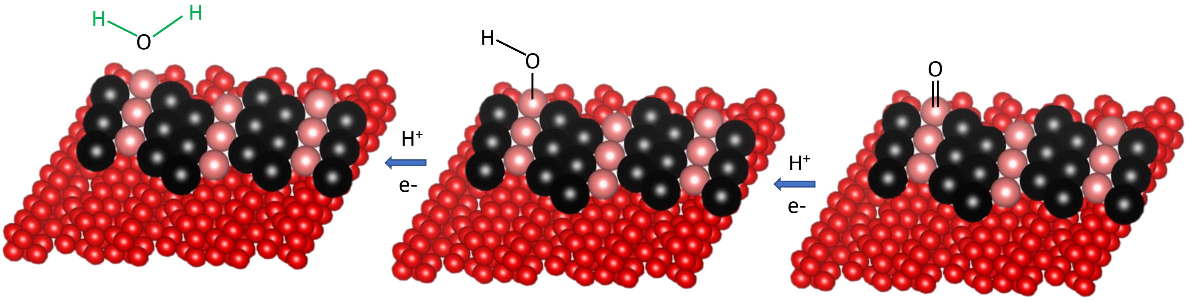

Fig. S23 | Regeneration of the catalyst after catalysis. 'Mo=O' bond further gets reduced to water via proton coupled electron transfer pathway and regenerate composite photocatalyst.

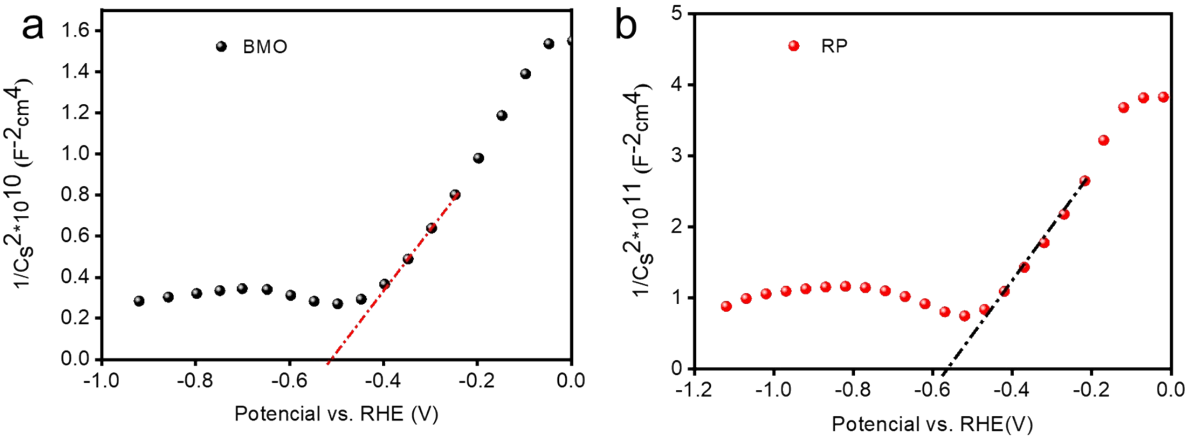

Fig. S24 | Electrochemical band edge measurements by Mott-Schottky plot. Conduction band edge was checked by determining flat band potential of Bi_2MoO_6 **(a)**, RP **(b).** Negative slope of the materials confirms nature of the semiconductor is n-type.

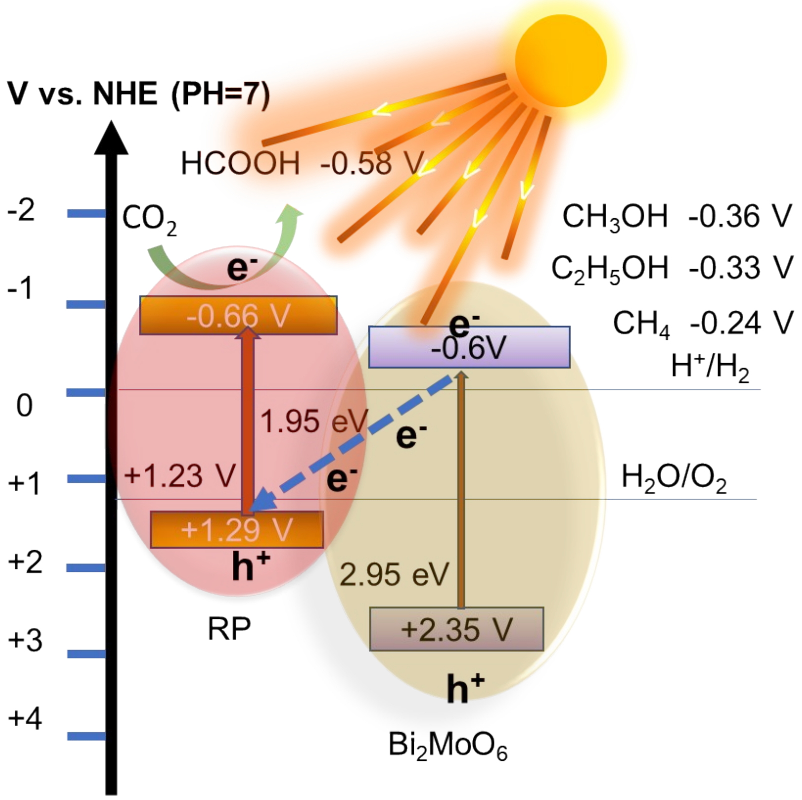

Fig. S25 | Charge transfer by Z-scheme mechanism. Schematic illustration of Z-scheme mechanism. The photogenerated electrons at the CBM of Bi_2MoO_6 travel to the VBM of the RP and then consequently recombine with the photogenerated holes. Meanwhile, the photogenerated electrons and holes are left, respectively, at the CBM of RP and VBM of Bi_2MoO_6 perform reduction and oxidation respectively.

References

1. W.-J. Li, S.-L. Chou, J.-Z. Wang, H.-K. Liu and S.-X. Dou, *Nano Lett.*, 2013, **13**, 5480-5484.
2. T. Oshima, S. Nishioka, Y. Kikuchi, S. Hirai, K.-i. Yanagisawa, M. Eguchi, Y. Miseki, T. Yokoi, T. Yui, K. Kimoto, K. Sayama, O. Ishitani, T. E. Mallouk and K. Maeda, *J. Am. Chem. Soc.*, 2020, **142**, 8412-8420.
3. A. Cherevotan, J. Raj, L. Dheer, S. Roy, S. Sarkar, R. Das, C. P. Vinod, S. Xu, P. Wells, U. V. Waghmare and S. C. Peter, *ACS Energy Lett.*, 2021, **6**, 509-516.
4. H. Li, S. Gan, H. Wang, D. Han and L. Niu, *Adv. Mater.*, 2015, **27**, 6906-6913.
5. M. Cheng, S. Yang, R. Chen, X. Zhu, Q. Liao and Y. Huang, *Int. J. Hydrogen Energy*, 2017, **42**, 9722-9732.
6. Y. Liu, B. Huang, Y. Dai, X. Zhang, X. Qin, M. Jiang and M.-H. Whangbo, *Catal. Commun.*, 2009, **11**, 210-213.
7. H. Maimaitizi, A. Abulizi, K. Kadeer, D. Talifu and Y. Tursun, *Appl. Surf. Sci.*, 2020, **502**, 144083.
8. W. Dai, H. Xu, J. Yu, X. Hu, X. Luo, X. Tu and L. Yang, *Appl. Surf. Sci.*, 2015, **356**, 173-180.
9. W. Dai, J. Yu, Y. Deng, X. Hu, T. Wang and X. Luo, *Appl. Surf. Sci.*, 2017, **403**, 230-239.
10. W. Dai, W. Xiong, J. Yu, S. Zhang, B. Li, L. Yang, T. Wang, X. Luo, J. Zou and S. Luo, *ACS Appl. Mater. Interfaces*, 2020, **12**, 25861-25874.
11. B. Cai, J. Wang, S. Gan, D. Han, Z. Wu and L. Niu, *J. Mater. Chem. A*, 2014, **2**, 5280-5286.
12. Y. He, Y. Wang, L. Zhang, B. Teng and M. Fan, *Appl. Catal., B*, 2015, **168-169**, 1-8.
13. W. Dai, J. Yu, S. Luo, X. Hu, L. Yang, S. Zhang, B. Li, X. Luo and J. Zou, *Chemical Engineering Journal*, 2020, **389**, 123430.
14. X. Chen, C. Zhuang, X. Wang, A. Liao, L. Li, Q. Liu, Y. Tang, C. Wu, Q. Shen and Z. Yu, *ACS Applied Energy Materials*, 2018, **1**, 6857-6864.
15. W. Dai, J. Yu, Y. Deng, X. Hu, T. Wang and X. Luo, *Applied Surface Science*, 2017, **403**, 230-239.
16. S. Li, C. Wang, D. Li, Y. Xing, X. Zhang and Y. Liu, *Chem. Eng. J.*, 2022, 135133.
17. W. Dai, J. Yu, H. Xu, X. Hu, X. Luo, L. Yang and X. Tu, *CrystEngComm*, 2016, **18**, 3472-3480.
18. Y.-F. Xu, M.-Z. Yang, B.-X. Chen, X.-D. Wang, H.-Y. Chen, D.-B. Kuang and C.-Y. Su, *J. Am. Chem. Soc.*, 2017, **139**, 5660-5663.